Hugoniot and Release Measurements in Diamond Shocked up to 26 Mbar

Introduction

The behavior of carbon at millions to billions of atmospheres of pressure is integral to evolution models for many solar and extrasolar planets (Uranus, Neptune, 55 Cancri E)[1,2] and white dwarf stars.[3,4] In Uranus and Neptune, carbon exists in the form of methane (CH_4) ice at the surface but may be in its elemental form near the core, where pressures and temperatures reach ~8 Mbar and ~8000 K, respectively.[5,6] Theoretical predictions suggest that the interiors of Uranus, Neptune, or Neptune-like exoplanets might contain diamond or even liquid oceans of carbon.[1,5] This strongly motivates studies of carbon's high-pressure response in both its solid and liquid phases.[7–9]

Carbon's equation of state (EOS) is also important to developing predictive models for inertial confinement fusion (ICF) experiments, where diamond shells are used to contain and compress the hydrogen fuel.[10] An ICF implosion uses a series of finely tuned shock waves to precompress the shell (ablator) and fuel. This initiates near isentropic compression while adding the desired amount of entropy needed to hydrodynamically stabilize the main implosion. An optimal target design is a delicate balance between these two effects. The diamond used in ICF targets is polycrystalline with grain sizes of ~10 nm (Refs. 11 and 12). The low surface roughness and isotropic character of this nanocrystalline diamond (NCD) compared to single-crystal diamond (SCD) makes NCD less susceptible to hydrodynamic instabilities seeded by crystal anisotropy at the ablator/fuel interface. Current implosion designs melt the NCD with the first shock to further limit instability growth. Modeling an ICF implosion requires accurate knowledge of NCD's response to multimegabar shocks and its behavior when it releases from these extreme pressures into the low-density fuel.

To date, data for carbon above the diamond melt boundary are limited to shock-compression measurements.[13–15] None of these data include NCD; high-precision measurements (relative density error < 1.5%) for SCD exist up to only 18 Mbar (Ref. 15). Shock Hugoniot data in solid diamond[16–18] and the solid–liquid coexistence region[7,8,15] are supplemented by ramp-compression measurements,[19,20] which are used to explore matter at temperatures significantly lower than temperatures on the Hugoniot. Ramp-compression data exist up to 8 Mbar in solid SCD[20] and 50 Mbar for solid NCD,[19] but theories describing liquid carbon above 18 Mbar are unconstrained by high-precision experiments. The experiments presented here provide high-pressure (up to 26 Mbar) shock-compression and release data for both full-density SCD ($\rho_0 = 3.515$ g/cm^3) and the lower-density NCD ($\rho_0 \sim 3.36$ g/cm^3) used in ICF capsules. The Hugoniot data provide a clear constraint on the pressure, density, and internal energy of liquid carbon, while the release data constrain the isentropes from these high-pressure, high-temperature shock states to a several-fold drop in pressure.[21,22]

Single-shock Hugoniot data for diamond (both SCD and NCD) were collected to 26 Mbar using impedance-matching (IM) techniques with quartz as a reference material. These new SCD data agree with density-functional theory molecular dynamics (DFT-MD) calculations for liquid carbon.[23] The data for NCD, which are expected to be at a slightly higher temperature, exhibit a compressibility that is even stiffer than shock-compressed SCD measurements and DFT-MD predictions. The NCD data suggest that, in addition to carbon's anomalously stiff fluid state, either its thermal properties are inadequately understood or the shock compression of NCD undergoes an additional (frictional) heating explained by its slightly lower density.

The release data were collected by releasing shock-compressed diamond into several lower-impedance materials with known shock Hugoniots including quartz,[24,25] CH,[26] silica foam,[25,27] and liquid D_2 (Refs. 28 and 29). This technique was previously used by Knudson, Desjarlais, and Pribram-Jones to benchmark the release of shocked quartz[25] and aluminum.[29] Data were acquired for diamond releasing from 8 to 20 Mbar, so release paths originated from both the coexistence region and liquid phase. The release data mostly agree with predictions using existing EOS models that do not include strength effects, indicating that strength does not largely affect the diamond release physics at these pressures. The release measurements into the low-density liquid D_2 are particularly valuable for

constraining ICF models since liquid D_2 is a good surrogate for the deuterium–tritium fuel in an ICF target.

The following sections describe the experimental design, targets, and diagnostics used in the laser-driven shock experiments; show the IM technique used to measure Hugoniot and release states; and present the NCD data analysis techniques followed by the results.

Experimental Technique

The experiments were performed at the Omega Laser Facility, a Nd:glass laser that is frequency tripled to a wavelength of 351 nm (Ref. 30). The experiments used 6 to 12 beams having temporally square pulses with durations of 2, 3, or 3.7 ns with total energies between 1.1 and 3.7 kJ. The beams with an 876-μm-diam laser focal spot were smoothed by spectral dispersion[31] and distributed phase plates.[32] On-target laser intensities of 0.66 to 3.3×10^{14} W/cm^2 were achieved, producing shock pressures up to 26 Mbar in the diamond targets.

The NCD targets were designed to provide both Hugoniot and release measurements on each shot. The targets [Fig. 148.1(a)] comprised a CH ablator, a Z-cut α-quartz standard (pusher), and an NCD sample glued to the pusher's rear surface. IM data were obtained at this interface for NCD Hugoniot measurements. A standard material [quartz, polystyrene (CH), SiO$_2$ foam, or liquid D_2] was in contact with the rear side of the NCD sample to determine its release behavior.

Adjacent to the NCD sample, a quartz witness provided a reference for the temporal history of the shock velocity. The witness was required because internal scattering attributed to the nanometer-sized diamond grains and their random orientations make NCD opaque to visible light.[12] For this reason, shock velocities in the NCD were measured from transit times. To facilitate these measurements, the NCD sample and rear standard were positioned to provide an unobstructed view of ~100 μm of the rear quartz pusher and NCD faces as shown in Figs. 148.1(a) and 148.1(b).

Examples of planar cryogenic and warm SCD target designs are shown in Fig. 148.2. SCD is transparent, obviating the need for the quartz witness, which allowed us to use one to three rear standards to obtain multiple release measurements on a single shot. Hugoniot measurements were made at the quartz/SCD interface and release measurements were made at the SCD/rear-standard interfaces. A thin (0.3- or 2-μm) gold layer was deposited on the rear of the CH ablator in some targets to help prevent preheat in the SCD and standards. A quartz baseplate (30 to 50 μm thick) was attached to the front side of the diamond whenever a gold layer was not used.

The NCD targets used nanocrystalline diamond (fabricated by Diamond Materials GmbH) identical to those used in ICF targets at the National Ignition Facility (NIF).[33] The density of the NCD samples was determined to be 3.360 ± 0.002 g/cm^3 using an Archimedes' measurement of a larger reference
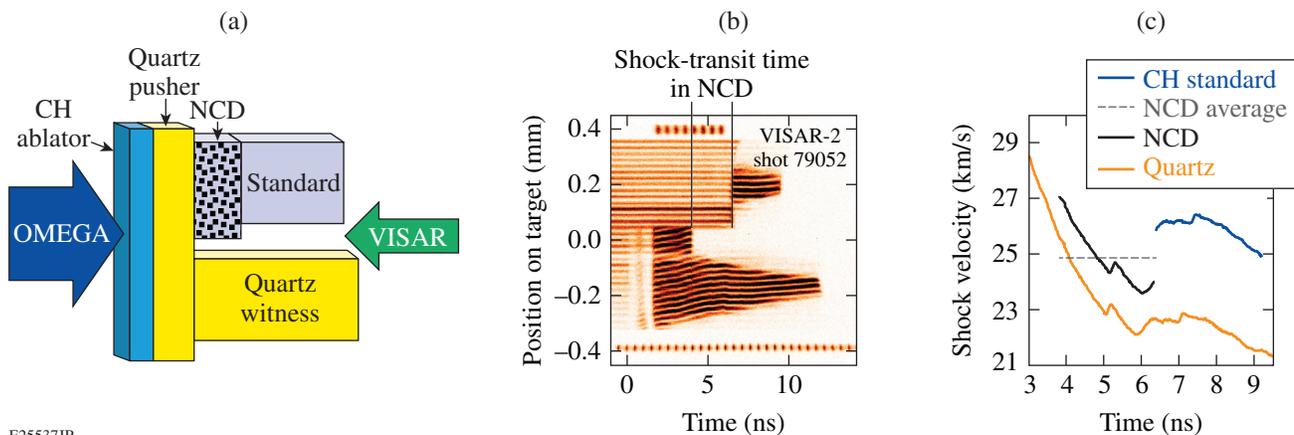
Figure 148.1

(a) The nanocrystalline diamond (NCD) target design comprising a CH ablator, a quartz pusher and witness, an NCD sample, and a standard positioned to facilitate measurements of transit times. (b) Raw VISAR (velocity interferometer system for any reflector) data from an experiment using the target design in (a). (c) Extracted shock velocities from (b). The shock-velocity profile in NCD (black line) was inferred from the average shock velocity (dashed line) and the observed shock-velocity profile in the adjacent quartz witness (orange line) using the nonsteady waves correction.[34] The shock-velocity profile in the CH standard (solid blue line) is observed once the shock breaks out of the NCD.

(a)

(b)
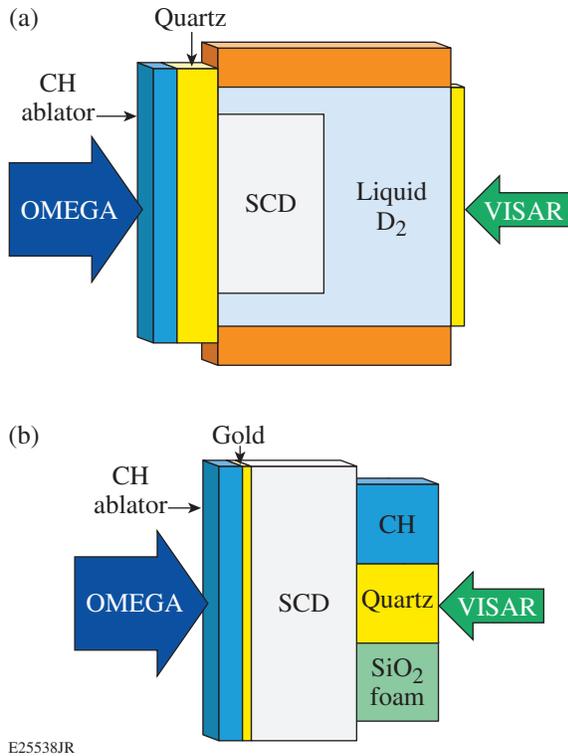
E25538JR

Figure 148.2

Schematics of (a) planar cryogenic and (b) warm targets used in single-crystal diamond (SCD) Hugoniot and release experiments. Targets had a CH ablator and one to three standards (liquid D_2, CH, quartz, or SiO_2 foam) on the rear side of the SCD.

sample from the same batch.[12] The SCD foils obtained from Applied Diamond had a density of ρ_0 = 3.515 g/cm^3 and were natural with a $\langle 110 \rangle$ orientation or fabricated with chemical vapor deposition (CVD) with a $\langle 100 \rangle$ orientation. The quartz (ρ_0 = 2.65 g/cm^3), CH (ρ_0 = 1.05 g/cm^3), and SiO_2-foam ($\rho_0 \sim$ 0.2g/cm^3) pieces (see Table 148.I for exact values) were obtained from Schafer Corporation. The planar cryogenic targets [Fig. 148.2(a)] comprised a liquid D_2–filled, cylindrical copper cell sealed with quartz on both faces. The initial D_2 density was determined from the temperature in the cryogenic cell and varied between 0.170 and 0.174 g/cm^3 on a shot-to-shot basis.[35] The uncertainty in the SiO_2 foam density was estimated to be ~2%, and uncertainties in the SCD, quartz, CH, and liquid D_2 densities were assumed to be negligible.

The shock velocities for impedance matching were measured using the line-imaging velocity interferometer system for any reflector (VISAR) described in Ref. 36. Opposite the drive beams, the VISAR probe beam is incident on the rear side of the target and the reflected signal is relayed to a pair of

interferometers. A delay etalon is inserted into one leg of each interferometer so that changes in Doppler shifts of the reflected probe beam, corresponding to moving reflective interfaces, are registered as fringe shifts in the interference pattern. The fringe shifts are proportional to the velocity of the moving interface through the velocity per fringe (VPF), which depends inversely on the etalon thickness and the index of refraction of the target medium at the 532-nm probe wavelength. The indices of refraction for the target materials at 532 nm were 2.42 (SCD), 1.55 (quartz), 1.59 (CH), 1.04 (0.2-g/cm^3 SiO_2 foam),[27] and 1.14 (0.174-g/cm^3 liquid D_2) (Ref. 28).

The two interferograms, which are recorded on separate streak cameras, provide time histories of the velocity of moving interfaces with ~10-ps resolution.[36] Fringe jumps or 2π phase ambiguities between the two records are resolved by using etalons of different thicknesses. The velocities presented here for the NCD Hugoniot and all release measurements are those measured using the more-sensitive VISAR leg. Measurements using the less-sensitive VISAR leg are presented for some SCD Hugoniot measurements because it provided better-resolved fringe shifts of the rapidly decaying shock at the quartz/SCD interface. Errors were estimated to be the larger of 5% of a fringe using the more-sensitive leg or the difference between the velocity from the more-sensitive leg and the weighted velocity average from both legs. An example of raw VISAR data and the extracted shock velocities from an NCD experiment using the target design in Fig. 148.1(a) are shown in Figs. 148.1(b) and 148.1(c). The VISAR diagnostic provides 1-D spatial resolution along the slit of the streak camera so that shock velocities are observed over an ~800-μm slice of the target.

The targets were shock compressed to a metallic fluid state producing a reflective shock front. VISAR recorded the shock velocity as a function of time in the transparent materials.[36] In opaque materials, the VISAR probe beam cannot reach the shock front within the target. Instead, VISAR registers the time that the shock breaks out of the opaque material. For example, the shock transit time in the NCD sample is given by the time between the two vertical lines in Fig. 148.1(b). The first time is registered by the arrival of the shock at the rear of the quartz pusher. The second time is registered from its arrival at the rear NCD interface. For transparent materials, higher-precision, *in-situ*, time-varying shock-velocity profiles were measured. A streaked optical pyrometer[37] (SOP) with an ~5-ps temporal resolution provided additional measurements of shock transit times. Average velocities in NCD were corrected using the nonsteady waves model discussed below.

Table 148.I: Diamond release data. All the single-crystal diamond (SCD) samples had a $\langle 110 \rangle$ orientation except for the SCD in shot 73733, which had a $\langle 100 \rangle$ orientation. U_s^C and U_s^{Stan} are the shock velocities at the interface between the diamond and the lower-impedance standard (quartz, CH, silica foam, or liquid D_2). U_s^{Stan} was corrected to account for the glue layer (when necessary) by linearly fitting to the measured shock velocity in the standard over a small time interval and extrapolating the fit backward across the glue layer. The initial densities of the liquid D_2 and foam samples are given in mg/cm^3 in column 3.

Shot	Diamond Type	Standard	U_s^C (km/s)	U_s^{Stan} (km/s)
77003	SCD	D_2 (174)	29.47±0.06	38.60±0.27
77848	SCD	D_2 (170)	28.56±0.06	36.86±0.12
77851	SCD	D_2 (170)	27.39±0.09	34.49±0.12
77856	SCD	D_2 (170)	29.10±0.06	37.83±0.13
79050	SCD	D_2 (174)	25.03±0.10	30.14±0.33
79053	SCD	D_2 (172)	24.62±0.10	29.29±0.22
73733	SCD	quartz	25.88±0.06	24.52±0.09
75397	SCD	quartz	23.67±0.07	21.63±0.15
75399	SCD	quartz	23.87±0.07	21.92±0.11
75400	SCD	quartz	23.20±0.11	21.05±0.16
75402	SCD	quartz	23.93±0.07	21.77±0.11
75404	SCD	quartz	29.05±0.7	27.61±0.11
77857	SCD	quartz	31.60±0.06	30.17±0.09
77859	SCD	quartz	31.57±0.06	30.05±0.09
77860	SCD	quartz	29.33±0.06	28.29±0.09
75397	SCD	CH	23.48±0.07	24.00±0.10
75399	SCD	CH	23.84±0.13	24.94±0.12
75400	SCD	CH	23.20±0.07	23.36±0.15
75404	SCD	CH	28.77±0.07	32.00±0.11
77857	SCD	CH	31.64±0.06	35.37±0.09
77859	SCD	CH	31.46±0.06	35.08±0.10
77860	SCD	CH	29.20±0.06	32.46±0.09
75397	SCD	foam (191)	23.63±0.07	25.01±0.16
75400	SCD	foam (191)	23.10±0.07	24.83±0.16
77004	NCD	D_2 (173)	26.68±0.82	33.29±0.12
77006	NCD	D_2 (172)	30.81±0.96	40.19±0.12
77002	NCD	quartz	31.21±0.45	30.11±0.09
77007	NCD	quartz	28.09±0.32	26.48±0.09
79048	NCD	quartz	22.16±0.18	20.44±0.16
77005	NCD	CH	28.09±0.33	31.90±0.09
77861	NCD	CH	25.76±0.31	27.92±0.10
77862	NCD	CH	24.48±0.26	26.25±0.09
79052	NCD	CH	23.94±0.16	25.87±0.16
79056	NCD	CH	26.57±0.28	28.93±0.16
79060	NCD	CH	22.93±0.20	24.87±0.25
79051	NCD	foam (198)	23.51±0.25	26.22±0.24

NCD: nanocrystalline diamond

Impedance-Matching Technique

Both Hugoniot and release states in diamond were measured using impedance matching (IM). The IM technique closes the Rankine–Hugoniot equations[22] to solve for pressure (P), density (ρ), and specific internal energy (E) in a shock-compressed material:

$$\rho_0 U_s = \rho \left(U_s - u_p \right), \qquad (1)$$

$$P = P_0 + \rho_0 U_s u_p, \qquad (2)$$

$$E = E_0 + \frac{1}{2} (P + P_0) \left(\frac{1}{\rho_0} - \frac{1}{\rho} \right). \qquad (3)$$

These equations describe the jump conditions across a shock front, where U_s is the shock velocity, u_p is the particle velocity, and states upstream of the shock are characterized by the subscript 0 (Ref. 22). By measuring U_s and u_p, the kinematic EOS parameters P, ρ, and E can be determined. In these experiments, U_s is measured using VISAR and u_p is determined using the IM technique, which relies on the equilibration of P and u_p at the interface between the material of interest (diamond) and a material with a known EOS. This method for measuring the Hugoniot and release behavior is described in the following two sections.

1. Hugoniot Measurements

The Hugoniot of an uncharacterized sample is measured with knowledge of the standard's EOS and the shock velocities about the standard/sample interface. In this work, the diamond Hugoniot data were measured using a quartz standard.[24,25] The pressure and particle velocity in the shocked quartz at the quartz pusher/diamond interface are given by the intersection of the Rayleigh line [Eq. (2)] and the quartz Hugoniot (cubic form taken from Ref. 25). When the shock crosses into the diamond, the pressure and particle velocity are continuous at the contact interface to maintain equilibrium. Since diamond has higher impedance ($\rho_0 U_s$), the quartz is re-shocked to a higher pressure, off its principal Hugoniot, to reach this new (P, u_p) state. This state, given by the intersection in the P–u_p plane of the quartz re-shock and the diamond Rayleigh line, marks a state on the diamond's Hugoniot.

The quartz re-shock was modeled using a Mie–Grüneisen EOS of the form

$$P = P_H + \Gamma \rho (E - E_H) \qquad (4)$$

with

$$E - E_H = \frac{1}{2} (P + P_H) \left(\frac{1}{\rho_1} - \frac{1}{\rho} \right), \qquad (5)$$

where P_H and E_H are the pressure and specific internal energy, respectively, on the quartz principal Hugoniot, ρ_1 is the density in the singly shocked quartz upstream of the re-shock, and ρ, P, and E are the density, pressure, and specific internal energy, respectively, in the re-shocked quartz. This re-shock model used the same reference Hugoniot P_H and effective Grüneisen parameter $\Gamma = \Gamma_{eff}$ as the quartz release model described in Ref. 25. It should be noted that P_H and Γ_{eff} are not necessarily physical; they were optimized such that the quartz release model matched experimental data and first-principles molecular dynamics (FPMD) simulations. This same construct should be accurate for modeling the re-shock since the quartz compresses only 20% to 30%. Indeed, the diamond P–u_p data determined by this model are only 1% to 2% higher than those obtained using the simple reflected Hugoniot approximation.

2. Release Measurements

The release behavior of shocked diamond was measured by impedance matching between diamond and several lower-impedance standards. The initial and final states of the diamond release are determined using the known Hugoniots of the diamond materials (measured previously or in this study) and those of the standards. By using various lower-impedance standards, the diamond release is measured at incrementally lower end-state pressures, mapping the release path in P–u_p space.

The release standards used in these experiments have been suitably characterized: quartz,[24,25] CH,[26] silica foam,[25,27] and liquid D_2 (Refs. 28 and 29). The diamond–D_2 IM data are particularly valuable to ensuring that the initial stages of an ICF implosion set the fuel on the correct adiabat for an optimal implosion.

The CH and liquid-D_2 Hugoniot fits used in this work were re-analyzed using new data for the standards used in those IM studies. The CH Hugoniot data from Barrios,[26] which used a quartz standard, were re-analyzed using the updated quartz Hugoniot and release model from Knudson and Desjarlais.[25] Similarly the liquid-D_2 Hugoniot data from Hicks,[28] which used an aluminum standard, were re-analyzed by Knudson *et al.* and presented in Ref. 29. The liquid-D_2 Hugoniot from the Hicks experiments was used in this analysis because both works were performed on the OMEGA laser and had the same initial densities to within 2.5%. Because the Hicks Hugoniot fit was determined for $\rho_0 = 0.174$ g/cm^3, the $U_s^{D_2}$ data plotted

here were normalized to that initial density using the corrective term $2.29\left(1-\rho_0\big/\rho_0^{\text{Hicks}}\right)$. This offset was determined in Ref. 28 by comparing the effect of ρ_0 on the Hugoniots that were modeled using the stiffest and softest D_2 EOS tables; it affected this data set by only <0.2%.

Shock velocities in diamond and the standards were measured at the IM interface and are presented in Table 148.I. The shock velocity in diamond at the point of breakout into the standard was measured directly from the VISAR data in SCD and inferred from the nonsteady wave correction in NCD. The shock velocity in the standard was extrapolated backward across the glue layer to this same point. The extrapolation was done by linearly fitting to the measured shock velocity over a 150- to 500-ps time interval when the shock first entered the standard. *HYDRA* simulations for a different shock experiment involving a quartz/LiH interface with a 0-, 2-, and 4-μm-thick oil layer between them showed that extrapolating the shock velocity backward across the entire oil (or glue) layer (as opposed to midway) most accurately represented shock behavior at the interface when the two materials were in direct contact.[38] Only data with steady or smoothly decaying shocks over 150 ps on both sides of the interface were used in the release analysis.

NCD Data Analysis

EOS data obtained from impedance matching require accurate measurements of shock velocities and error propagation to provide high-confidence data. Modern VISAR systems can provide <1% velocity measurements in transparent samples,[36] yielding precise EOS data.[26] Opaque or translucent samples like NCD present a considerably different challenge. The methods used to obtain average shock velocities (i.e., transit times) and to correct those velocities for unsteadiness are described below.

1. Measurements of Shock Transit Times

Average shock velocities in the NCD samples were determined using the measured thicknesses and shock transit times presented in Table 148.II. VISAR and SOP were used to measure the times that the shock exited the quartz pusher (t_1) and the NCD (t_2). This defined the total time ($\Delta t_{\text{total}} = t_2 - t_1$) that the shock spent in the NCD sample and the glue layer preceding it. The transit time across the NCD sample alone is calculated by

$$\Delta t_{\text{NCD}} = \Delta t_{\text{total}} - \Delta x_{\text{glue}}\big/U_s^{\text{glue}},$$

where Δx_{glue} is the estimated glue thickness (described in **Measurements of Thickness**, below) and U_s^{glue} is the shock

velocity in the glue estimated using the *SESAME* 7603 table for epoxy and the known pressure and particle velocity at the quartz pusher/glue interface.

For targets with an uncovered NCD step, as shown in Fig. 148.1(a), shock breakout times were measured using the drop in the VISAR reflectivity across the step/vacuum interface seen in Fig. 148.1(b). The peak in the derivative of the reflectivity, denoting the steepest slope in the drop in signal, defined the shock breakout time. This method yielded the most-consistent and most-precise transit times since the peaks were measured to ~5 ps. For targets without the steps, breakout times were defined by the rapid change in thermal emission recorded by the SOP at the quartz pusher/glue/witness interface (t_1) and the NCD/glue/standard interface (t_2). The steepest slope of the SOP signal was used to define t_1 and t_2. An additional uncertainty up to 50 ps was applied to these measurements because the location of the peak defining t_1 or t_2 was not as consistent since it varied with the thickness of the glue layer. The SOP signal does not drop to zero at the glue (or liquid D_2) interface, as was observed in the VISAR reflectivity at the step/vacuum interface. As the shock approached the rear surface of the NCD sample, the VISAR reflectivity and the SOP signal increased exponentially because of reduced volumetric scattering. This contributed to the uncertainty in t_2 because the emission continuously increased across the NCD/glue/standard (or liquid D_2) interface.

2. Measurements of Thickness

The step heights of the NCD samples glued to the quartz pushers (Δx_{total}) were measured using white-light interferometry with a Zygo NexView 3-D optical surface profiler. The average NCD step height was referenced to the quartz pusher in the areas where the breakout times were measured. The glue thicknesses were estimated by combining these measurements with the thickness profiles of the individual samples (Δx_{NCD}), measured using a dual confocal microscope. Glue layers were kept to ~1 μm and are defined by $\Delta x_{\text{glue}} = \Delta x_{\text{total}} - \Delta x_{\text{NCD}}$. For some targets, Δx_{glue} was set to 0 μm because a negative glue thickness was inferred; the uncertainty always permitted a positive glue thickness. The average shock velocity in NCD alone was determined using $\left\langle U_s^{\text{NCD}}\right\rangle = \left(\Delta x_{\text{total}} - \Delta x_{\text{glue}}\right)\big/\Delta t_{\text{NCD}}$.

3. Nonsteady Wave Correction

In laser-driven experiments, steady shocks are difficult to attain because of the expanding ablation plasma. A technique for correcting the average shock velocity to account for nonsteadiness was developed for use in laser-driven experiments.[34] For a large planar drive, the shock-velocity history in an opaque sample is related to and corrected by the observed history in

Table 148.II: NCD transit time data and Hugoniot data from impedance matching (IM) with a quartz standard. The shock transit times (Δt_{total}) and thicknesses (Δx_{total} and Δx_{NCD}), where "total" denotes the combined NCD sample and preceding glue layer, were used to determine the average shock velocity in NCD ($\langle U_s^{NCD} \rangle$). $\langle U_s^{NCD} \rangle$ was corrected using the method described in **Nonsteady Wave Correction** (p. 164) to determine $U_s^{NCD}(t_1)$ at the IM interface. The shock velocity in quartz $[U_s^{Q}(t_1)]$ and $U_s^{NCD}(t_1)$ were used in the IM analysis to determine the particle velocity (u_p^{NCD}), pressure (P^{NCD}), and density (ρ_{NCD}) on the NCD Hugoniot.

Shot	Δt_{total} (ns)	Δx_{total} (μm)	Δx_{NCD} (μm)	$\langle U_s^{NCD} \rangle$	$U_s^{Q}(t_1)$	$U_s^{NCD}(t_1)$	u_p^{NCD}	P^{NCD} (Mbar)	ρ^{NCD} (g/cm³)
77001	2.035±0.020	64.24±0.44	63.29±0.45	31.10±0.36	29.54±0.09	31.25±0.36	17.62±0.13	18.50±0.17	7.71±0.17
77002	1.890±0.023	62.27±0.38	61.89±0.29	32.75±0.45	31.59±0.09	33.03±0.42	19.29±0.16	21.40±0.22	8.08±0.22
77004*	2.384±0.069	64.80±0.54	64.97±0.50	27.19±0.82	25.94±0.09	27.79±0.80	14.86±0.18	13.87±0.26	7.25±0.34
77005	2.082±0.020	63.03±0.31	62.69±0.28	30.10±0.33	30.17±0.09	31.26±0.31	18.25±0.13	19.17±0.16	8.07±0.17
77006*	2.051±0.063	64.19±0.23	63.31±0.50	30.89±0.96	29.27±0.09	31.20±0.96	17.36±0.23	18.19±0.36	7.61±0.41
77007	2.109±0.019	63.44±0.39	63.71±0.33	30.08±0.32	29.81±0.09	31.28±0.31	17.88±0.12	18.80±0.16	7.85±0.14
77861	2.263±0.021	63.06±0.43	62.61±0.30	27.67±0.31	27.44±0.09	28.89±0.29	16.11±0.11	15.63±0.13	7.60±0.14
77862	2.319±0.019	61.72±0.30	61.43±0.27	26.49±0.25	26.51±0.09	27.66±0.24	15.44±0.10	14.35±0.11	7.61±0.13
79048	2.704±0.011	62.18±0.41	62.14±0.27	22.97±0.17	23.57±0.17	24.52±0.17	13.29±0.16	10.95±0.15	7.34±0.12
79049	1.951±0.008	62.07±0.48	62.17±0.26	31.79±0.26	33.87±0.16	35.10±0.26	20.98±0.21	24.74±0.27	8.36±0.17
79051	2.502±0.011	62.65±0.58	63.00±0.25	25.04±0.25	26.06±0.16	27.57±0.24	15.02±0.16	13.92±0.17	7.39±0.14
79052	2.517±0.011	63.58±0.30	62.45±0.34	24.81±0.15	25.61±0.16	27.06±0.15	14.69±0.15	13.36±0.15	7.35±0.11
79054	2.481±0.011	61.31±0.73	61.83±0.28	24.70±0.30	26.80±0.16	27.15±0.30	15.82±0.17	14.43±0.18	8.06±0.21
79055	2.263±0.010	61.54±0.68	61.39±0.25	27.11±0.30	28.22±016	29.70±0.31	16.67±0.17	16.63±0.19	7.66±0.17
79056	2.315±0.008	65.17±0.66	62.45±0.30	26.98±0.26	28.02±0.16	29.52±0.28	16.51±0.17	16.38±0.18	7.63±0.16
79057	2.196±0.010	61.60±0.44	61.22±0.25	27.87±0.22	28.56±0.16	29.93±0.22	16.97±0.17	17.07±0.18	7.76±0.15
79058	2.142±0.015	62.72±0.36	62.87±0.25	29.28±0.26	31.00±0.16	32.42±0.25	18.81±0.18	20.49±0.21	8.01±0.16
79059	2.398±0.010	61.66±0.46	61.84±0.25	25.70±0.21	26.91±0.16	28.40±0.21	15.65±0.16	14.94±0.16	7.49±0.13
79060	2.571±0.015	61.89±0.32	62.16±0.42	24.07±0.18	25.49±0.16	26.77±0.21	14.64±0.17	13.16±0.13	7.42±0.16
21233 (EP)	1.917±0.011	61.95±0.41	61.40±0.33	32.03±0.26	33.95±0.16	35.29±0.25	21.04±0.22	24.94±0.28	8.32±0.17
21237 (EP)	2.079±0.010	63.02±0.48	62.63±0.26	30.12±0.25	31.82±0.16	33.41±0.25	19.37±0.19	21.75±0.23	8.00±0.15

*Shots 77004 and 77006, which used liquid D_2–filled targets, were not included in the NCD Hugoniot fit because of the large uncertainty in measuring Δt_{total} from the lack of step/vacuum interfaces and contractions of the glue layers in the cryogenic cell.

an adjacent transparent witness.[34] This requires that the EOS of the witness and witness be known.

The amplitudes and temporal spacing of perturbations originating at the laser drive and arriving at the shock fronts in NCD and the adjacent quartz witness depend on their relative equations of state. Deviations from $\langle U_s^{NCD} \rangle$ are correlated to the observed velocity profile in the witness by $\delta U_s^{NCD}(t-t_1) = G \delta U_s^Q\left[(t-t_1)/F\right]$, where G and F are linear scaling factors that describe the relative amplitude and time history, respectively, of the shock-velocity profiles; δU_s^Q is the deviation from the average shock velocity in the quartz witness over the time period $\Delta t_{NCD}/F$, which corresponds to the same set of temporal perturbations experienced by the NCD; F is determined by the relative sound speeds and Hugoniots in the two materials; and G is additionally affected by the Grüneisen parameters. The quartz Hugoniot and $\Gamma = \Gamma_{eff}(U_s)$ were taken from Ref. 25, and quartz sound speeds were determined from the derivatives of the release paths calculated using that construct. Since the intention of this work was to measure the NCD Hugoniot, an iterative process was used where initial estimates for the Hugoniot, Γ's, and sound speeds were taken from a tabular EOS (LEOS 9061) (Ref. 23). This EOS model was chosen because the high-pressure SCD Hugoniot data best agree with LEOS 9061 predictions. The NCD velocity histories for the entire data set were first determined using the correction with these initial estimates. Then, impedance matching was done using the measured U_s^Q and inferred U_s^{NCD} at the IM interface to produce a linear U_s–u_p relation in NCD. The process was repeated using the updated Hugoniot fit so that the NCD velocity profiles were iteratively corrected until the linear U_s–u_p relation converged. An example of an NCD velocity history determined using this method is shown by the black curve in Fig. 148.1(c).

Velocity extrapolation across the glue layer at the quartz/ NCD interface was treated differently to take advantage of the quartz witness. A continuous velocity profile was inferred across the glue layer at the quartz pusher/witness interface. Using this interpolation, the velocity profile in the witness beginning at the time the shock enters the NCD,

$$\left(t_1 + \Delta x_{glue}/U_s^{glue}\right),$$

was used in the nonsteady wave correction to determine F and G. With knowledge of F and G,

$$U_s^{NCD}(t) = \langle U_s^{NCD} \rangle + G \delta U_s^Q\left[(t-t_1)/F\right]$$

was used to calculate the NCD shock velocities at times t_1 and t_2 needed for impedance matching.

Results

1. Hugoniot Data

a. SCD: The SCD Hugoniot data are listed in Table 148.III and plotted in Fig. 148.3 with existing diamond data by Knudson *et al.*[8] and Hicks *et al.*[15] The Knudson *et al.* experiments primarily used full-density (3.515-g/cm³) microcrystalline diamond and were performed using magnetically driven flyer-plate techniques. The Hicks experiments and this work, both IM experiments carried out using the OMEGA laser, used $\langle 110 \rangle$-oriented SCD and a quartz standard. The existing data in Fig. 148.3 suggest that *SESAME* 7830 best models the Hugoniot across the coexistence region (6 to 10.5 Mbar) and beyond the melt (>10.5 Mbar). This work measured less compressibility, however, than *SESAME* 7830 above 15 Mbar; this stiffer behavior is predicted by a DFT-MD EOS model (LEOS 9061).[23]

The Hicks data plotted in Fig. 148.3 are not the same as presented in the original publication; the data were re-analyzed using the updated quartz Hugoniot and the same re-shock formulation presented here. For a given pressure, this re-analysis decreased the density by ~3%. For $P^C > 20$ Mbar (corresponding to $P^Q > 16$ Mbar at the IM point), the quartz Hugoniot fit used in impedance matching was extrapolated to higher pressures than given in the quartz data set.[24,25] If the extrapolation of the quartz Hugoniot is not valid at higher pressure, this could contribute to the apparent stiffening of the Hugoniot data that relied on a quartz standard.

b. NCD: The NCD Hugoniot was measured between 10 and 25 Mbar. The data are presented in Table 148.II and plotted in the U_s–u_p and P–ρ planes in Fig. 148.4. The Hugoniot curves derived from the EOS tables in Fig. 148.4 were modeled using the appropriate lower initial density $\left(\rho_0^{NCD} = 3.36\, g/cm^3\right)$. The NCD U_s–u_p Hugoniot data are approximately linear and were fit to $U_s = a_0 + a_1(u_p - \beta)$, where the coefficients and their standard deviations are listed in Table 148.IV. An orthogonally weighted least-squares linear fit was taken about the centroid of the data (β) so that the uncertainties in a_0 and a_1 are uncorrelated.[39] The standard deviation in the fit is given by[39]

$$\sigma_{U_s}(u_p) = \left[\sigma_{a_0}^2 + \sigma_{a_1}^2\left(u_p - \beta\right)^2\right]^{1/2}.$$

The NCD data are slightly stiffer than predictions using LEOS 9061 [Fig. 148.4(b)], which well-represented the SCD

Table 148.III: $\langle 110 \rangle$ SCD Hugoniot data from impedance matching with a quartz standard.

Shot	U_s^Q	U_s^{SCD}	P^{SC} (Mbar)	U_p^{SCD}	ρ^{SCD} (g/cm^3)
79050	27.54±0.16	28.47±0.10	16.00±0.16	15.98±0.16	8.02±0.11
79053	28.68±0.16	29.56±0.10	17.51±0.17	16.85±0.16	8.17±0.12
77848	32.94±0.11	33.84±0.06	23.79±0.19	20.00±0.16	8.59±0.10
77858	33.17±0.09	34.07±0.06	24.15±0.18	20.16±0.15	8.61±0.10
77860	33.77±0.10	34.24±0.06	24.92±0.20	20.70±0.17	8.89±0.12
77851	34.62±0.09	35.06±0.06	26.27±0.24	21.32±0.19	8.97±0.13
77856	34.82±0.09	35.29±0.07	26.62±0.25	21.46±0.20	8.97±0.14

E25540JR
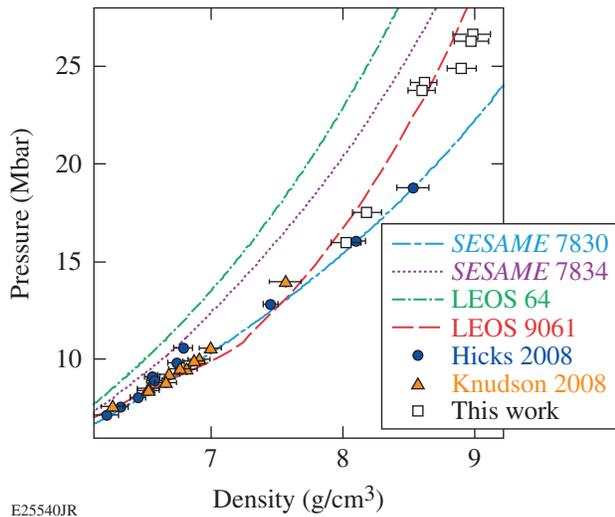
Figure 148.3
Full-density ($\rho_0 = 3.515$ g/cm^3) diamond Hugoniot data from this work (open squares), Knudson[8] (orange triangles), and Hicks[15] re-analyzed using the updated quartz equation of state (EOS)[25] (blue circles). The data are compared to Hugoniots modeled using diamond EOS tables.

E25539JR
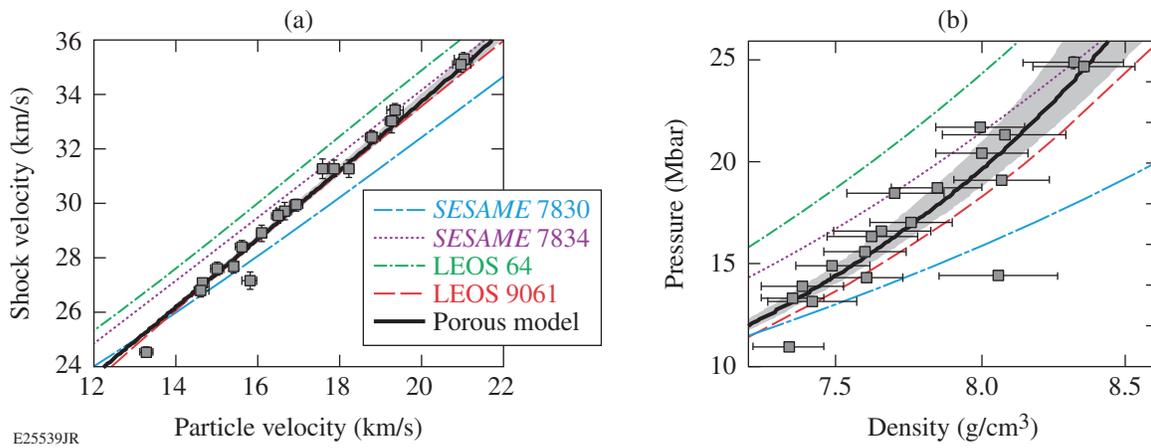
Figure 148.4
NCD ($\rho_0 = 3.36$ g/cm^3) Hugoniot data (gray squares) from impedance matching with a quartz standard. (a) The shock velocity versus particle velocity data and (b) the pressure versus density data are compared to Hugoniots modeled using diamond EOS tables and a porous model (solid black line) modeled using Eq. (6) with $\Gamma = 1.03$. The porous model using $\Gamma = 1.03 \pm 0.1$ is shown by the gray-shaded areas.

Table 148.IV: Coefficients and uncertainties to the orthogonally weighted least-squares fit to the NCD U_s–u_p data of the form $U_s = a_0 + a_1 (u_p$–$\beta)$.

a_0 (km/s)	a_1	β (km/s)	σ_{a_0}	σ_{a_1}
29.424	1.361	16.62	0.077	0.037

Hugoniot in the same pressure range (Fig. 148.3). NCD's lower initial density and reduced compressibility compared to SCD are consistent with that of a porous sample:

$$\left(m = \rho_0^{\text{SCD}} \big/ \rho_0^{\text{NCD}} = 1.046\right).$$

Porous samples exhibit stiffer and even "reverse" Hugoniots as a result of added entropy during the pore-collapse phase of compression.[22]

We find that NCD's Hugoniot can be described using a simple porosity model from McQueen[21] (black line in Fig. 148.4), given by

$$P_{\text{H}}^{\text{NCD}}(\rho) = P_{\text{H}}^{\text{SCD}}(\rho) \frac{1 - \dfrac{\Gamma}{2}\left(\dfrac{\rho}{\rho_0^{\text{SCD}}} - 1\right)}{1 - \dfrac{\Gamma}{2}\left(\dfrac{\rho}{\rho_0^{\text{NCD}}} - 1\right)}, \qquad (6)$$

where $P_{\text{H}}^{\text{SCD}}$ is the SCD Hugoniot, $\rho_0^{\text{SCD}} = 3.515$ g/cm^3, $\rho_0^{\text{NCD}} = 3.36$ g/cm^3, and $\Gamma = 1.03$. This model is derived from the definition of the Grüneisen parameter, such that the Hugoniots of the porous and crystal-density materials are related through Γ. The reference Hugoniot $\left(P_{\text{H}}^{\text{SCD}}\right)$ was established by fitting the SCD U_s–u_p Hugoniot data in the same high-pressure fluid region (>11 Mbar) as where the NCD data were obtained. This orthogonally weighted linear fit is given by $U_s = (30.018\pm0.057) + (1.208\pm0.020) (u_p$–$17.12)$. For simplicity, Γ was assumed to be constant and was optimized at 1.03. The range of the porous model using $\Gamma = 1.03\pm0.1$ is represented by the gray-shaded area in Fig. 148.4. $\Gamma \sim 1$ is ~20% higher than predicted by the DFT-MD model, which predicts $\Gamma \sim 0.8$ over the same density range as the data. This suggests that compared to the DFT-MD model, more energy goes into ΔP than other degrees of freedom for a given ΔE. This difference is related to the discrepancy between the DFT-MD Hugoniot (using ρ_0^{NCD}) and the NCD data despite agreement with the SCD Hugoniot data.

c. Error analysis: The values and errors in the Hugoniot data (Tables 148.II and 148.III) represent the mean and standard deviation of each parameter determined using a Monte Carlo error analysis with 10,000 runs for NCD and 100,000 runs for SCD. For each run, the observable parameters $\left(U_s^Q \text{ and } U_s^{\text{SCD}} \text{ for SCD, or } U_s^Q, \Delta x_{\text{NCD}}, \Delta x_{\text{total}}, \Delta t_{\text{total}}, \text{ and } \rho_0^{\text{NCD}}\right)$ for NCD) were varied within their error estimates. The cubic quartz U_s–u_p coefficients and Γ_{eff} used in impedance matching were varied once per run using the co-variance matrices listed in Ref. 25. For NCD, the nonsteady wave correction and impedance matching were done each time until convergence was met, yielding 10,000 possible sets of Hugoniot data. The total error bars in ρ^{NCD} are between 1.5% and 3%, with the dominating error caused by the uncertainty in target metrology and transit times.

2. Release Data

The diamond release data (Table 148.I) are plotted in Fig. 148.5 in terms of the observables, i.e., shock velocities on either side of the IM interface. The U_s^C and U_s^{Stan} data are shown for the release of diamond into liquid D$_2$, SiO$_2$ foam, CH, and quartz (the blue triangles, green diamonds, red squares, and orange circles, and respectively). The data are compared to the velocities predicted at the IM interface (lines) using the diamond EOS models. These lines were created using states on the diamond Hugoniot (abscissa) from which release paths were calculated. The intersections of release paths with the Hugoniot of the known standard provided the final states (ordinate).

The SCD release data in Fig. 148.5(a) show that *SESAME* 7830 (black lines) and LEOS 9061 (colored lines) are best for modeling the overall behavior of the diamond release at the pressures where their respective Hugoniots are most valid, i.e., *SESAME* 7830 below $U_s^C < 28$ km/s and LEOS 9061 above that velocity. The SCD data with $U_s^C < 24.4$ km/s, which corresponds to the completion of melt along the Hugoniot,[7] should be in the coexistence region upon release. The data do not deviate from the *SESAME* 7830 predictions, which do not include strength effects, indicating that strength does not play a significant role in the release from >8 Mbar. Shock-wave splitting into an elastic precursor and an inelastic wave should not occur until U_s^C decays below ~22.3 km/s in the ⟨110⟩ SCD and ~21.6 km/s in polycrystalline diamond,[16] and therefore should not affect the SCD or NCD data sets.

For the NCD [Fig. 148.5(b)], the data are well represented using a Mie–Grüneisen release model referencing the porous Hugoniot shown in Fig. 148.4 with a constant $\Gamma = 1.03$ along the
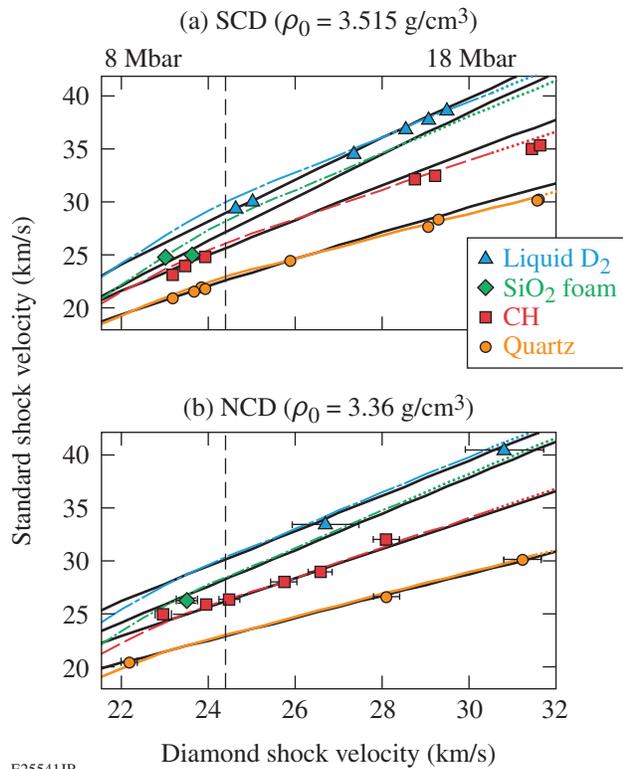
Figure 148.5

(a) SCD and (b) NCD release data compared to predictions using diamond EOS models and existing Hugoniot fits for the standards. Data points are shock velocities for diamond releasing into liquid D_2 (blue triangles), SiO_2 foam (green diamonds), CH (red squares), and quartz (orange circles). Predicted $U_s^C - U_s^{Stan}$ relationships using LEOS 9061 (colored lines) to model the diamond Hugoniot and release paths and existing Hugoniot fits for the standards: liquid D_2 (Refs. 28 ad 29) (dashed–dotted blue line), SiO_2 foam[27] (dashed–dotted green line), CH (Ref. 26) (dashed red line), and quartz[24,25] (solid orange line). Dotted portions of lines indicate that an extrapolation of the Hugoniot fit outside the standard's data range was used. The black lines in (a) are predicted $U_s^C - U_s^{Stan}$ relationships using *SESAME* 7830 to model the diamond Hugoniot and release paths. The black lines in (b) are predicted $U_s^C - U_s^{Stan}$ relationships using a Mie–Grüneisen model for the diamond Hugoniot and release paths with the same $\Gamma = 1.03$. The dashed vertical lines in (a) and (b) indicate the completion of melt on the diamond Hugoniot at 24.4($\pm$0.4) km/s (Ref. 7). For data to the left of the line, diamond released from the coexistence region. For data to the right of the line, diamond released from the liquid phase.

release path (black lines). This is consistent with the $\Gamma = 1.03$ used in the porous model that fits the Hugoniot data. LEOS 9061 (colored lines) is also adequate for predicting the release data, despite a slight 1% to 2% offset in inferred density for a given pressure on the initial Hugoniot state. The NCD data in the range $24 < U_s^{NCD} < 32$ km/s (~$12 < P^{NCD} < $~20 Mbar) release from an initial state where LEOS 9061 is within the error of the NCD Hugoniot measurements. While LEOS 9061

does not fully capture the NCD Hugoniot, it does represent the release data. This indicates that LEOS 9061 correctly models the NCD ablator's release into surrogate liquid D_2 fuel when the experimental liquid D_2 Hugoniot (Hicks[28] re-analyzed by Knudson[29]) is used. For comparison, the Kerley deuterium model[40] predicts faster shock velocities at the IM interface than the Hicks Hugoniot fit.

The NCD was most likely shocked into the liquid phase at the front NCD surface where the Hugoniot was measured. In the shots to the left of the melt line in Fig. 148.5(b), the shock decayed sufficiently enough during its transit that the NCD was at least partially solid upon release at its rear surface. This was apparent from the VISAR data of the unobstructed NCD step, which showed finite reflectivity at the NCD free surface after shock breakout, indicating a solid rather than a liquid state. The U_s^{Stan} data still follow the LEOS 9061 predictions, whereas when SCD released from the solid phase, the U_s^{Stan} data were slower than the LEOS 9061 predictions. Thermal effects from NCD's porosity could be contributing to the different response when NCD releases from the coexistence region.

Conclusions

The Hugoniot and release behavior of diamond were measured at multimegabar pressures and the Grüneisen parameter for high-pressure fluid carbon was extracted from the experimental data sets. These measurements are important to constrain models used in planetary astrophysics and to design ICF targets with NCD ablators. The SCD Hugoniot above 15 Mbar agrees with DFT-MD calculations (LEOS 9061) in liquid carbon. NCD's response to shock compression is slightly stiffer than that of SCD and the DFT-MD predictions, even when taking into account its lower initial density. This behavior can be described using a standard porosity model,[21] indicating that thermal effects from the initial pore collapse affect NCD's high-pressure Hugoniot. This effect must be included when using the EOS tables to model NCD. The stiffer NCD response compared to the DFT-MD EOS model (LEOS 9061) has implications for ICF target designs because additional heating raises the adiabat of the implosion. A Grüneisen parameter of ~1 in the liquid phase (11 to 26 Mbar) was derived from the experimental NCD and SCD Hugoniot fits. This value is consistent with a Mie–Grüneisen EOS that accurately models the NCD release data.

We measured two data points of NCD releasing into liquid D_2 and six SCD/liquid D_2 data points, which are especially valuable for constraining ICF models that describe the NCD ablator release into the hydrogen fuel.[41,42] The diamond–liquid

D_2 IM data can be reproduced when using the appropriate diamond EOS model (*SESAME* 7830 or LEOS 9061 based on the diamond type and U_s^C) and the experimental liquid D_2 Hugoniot.[28,29] Overall, the release response of both types of diamond are adequately modeled using existing EOS tables, which do not include strength effects. Strength may affect the diamond release behavior at lower pressure when the elastic precursor is separated from the main shock wave. Some difference in behavior exists between SCD and NCD when releasing from the coexistence region. Thermal effects from NCD's porosity could be the source of this difference.

ACKNOWLEDGMENT

REFERENCES

1. M. Ross, Nature **292**, 435 (1981).

2. N. Madhusudhan, K. K. M. Lee, and O. Mousis, Astrophys. J. Lett. **759**, L40 (2012).

3. H. M. Van Horn, *Unlocking the Secrets of White Dwarf Stars* (Springer International Publishing, Switzerland, 2015).

4. T. S. Metcalfe, M. H. Montgomery, and A. Kanaan, Astrophys. J. **605**, L133 (2004).

5. F. Ancilotto *et al.*, Science **275**, 1288 (1997).

6. T. Guillot, Annu. Rev. Earth Planet. Sci. **33**, 493 (2005).

7. J. H. Eggert, D. G. Hicks, P. M. Celliers, D. K. Bradley, R. S. McWilliams, R. Jeanloz, J. E. Miller, T. R. Boehly, and G. W. Collins, Nat. Phys. **6**, 40 (2010).

8. M. D. Knudson, M. P. Desjarlais, and D. H. Dolan, Science **322**, 1822 (2008).

9. A. A. Correa *et al.*, Phys. Rev. B **78**, 024101 (2008).

10. A. J. MacKinnon, N. B. Meezan, J. S. Ross, S. Le Pape, L. Berzak Hopkins, L. Divol, D. Ho, J. Milovich, A. Pak, J. Ralph, T. Döppner, P. K. Patel, C. Thomas, R. Tommasini, S. Haan, A. G. MacPhee, J. McNaney, J. Caggiano, R. Hatarik, R. Bionta, T. Ma, B. Spears, J. R. Rygg, L. R. Benedetti, R. P. J. Town, D. K. Bradley, E. L. Dewald, D. Fittinghoff, O. S. Jones, H. R. Robey, J. D. Moody, S. Khan, D. A. Callahan, A. Hamza, J. Biener, P. M. Celliers, D. G. Braun, D. J. Erskine, S. T. Prisbrey, R. J. Wallace, B. Kozioziemski, R. Dylla-Spears, J. Sater, G. Collins, E. Storm, W. Hsing, O. Landen, J. L. Atherton, J. D. Lindl, M. J. Edwards, J. A. Frenje, M. Gatu-Johnson, C. K. Li, R. Petrasso, H. Rinderknecht, M. Rosenberg, F. H. Séguin, A. Zylstra, J. P. Knauer, G. Grim, N. Guler, F. Merrill, R. Olson, G. A. Kyrala, J. D. Kilkenny, A. Nikroo, K. Moreno, D. E. Hoover, C. Wild, and E. Werner, Phys. Plasmas **21**, 056318 (2014).

11. J. Biener, D. D. Ho, C. Wild, E. Woerner, M. M. Biener, B. S. El-dasher, D. G. Hicks, J. H. Eggert, P. M. Celliers, G. W. Collins, and N. E. Teslich, Jr., Nucl. Fusion **49**, 112001 (2009).

12. C. Dawedeit *et al.*, Diam. Relat. Mater. **40**, 75 (2013).

13. H. Nagao *et al.*, Phys. Plasmas **13**, 052705 (2006).

14. S. Brygoo *et al.*, Nature Materials **6**, 274 (2007).

15. D. G. Hicks, T. R. Boehly, P. M. Celliers, D. K. Bradley, J. H. Eggert, R. S. McWilliams, R. Jeanloz, and G. W. Collins, Phys. Rev. B **78**, 174102 (2008).

16. R. S. McWilliams, J. H. Eggert, D. G. Hicks, D. K. Bradley, P. M. Celliers, D. K. Spaulding, T. R. Boehly, G. W. Collins, and R. Jeanloz, Phys. Rev. B **81**, 014111 (2010).

17. K. Kondo and T. J. Ahrens, Geophys. Res. Lett. **10**, 281 (1983).

18. M. N. Pavlovskii, Sov. Phys.-Solid State **13**, 741 (1971).

19. R. F. Smith, J. H. Eggert, R. Jeanloz, T. S. Duffy, D. G. Braun, J. R. Patterson, R. E. Rudd, J. Biener, A. E. Lazicki, A. V. Hamza, J. Wang, T. Braun, L. X. Benedict, P. M. Celliers, and G. W. Collins, Nature **511**, 330 (2014).

20. D. K. Bradley, J. H. Eggert, R. F. Smith, S. T. Prisbrey, D. G. Hicks, D. G. Braun, J. Biener, A. V. Hamza, R. E. Rudd, and G. W. Collins, Phys. Rev. Lett. **102**, 075503 (2009).

21. R. G. McQueen *et al.*, in *High-Velocity Impact Phenomena*, edited by R. Kinslow (Academic Press, New York, 1970).

22. Ya. B. Zel'dovich and Yu. P. Raĭzer, in *Physics of Shock Waves and High-Temperature Hydrodynamic Phenomena*, edited by W. D. Hayes and R. F. Probstein (Academic Press, New York, 1966).

23. L. X. Benedict *et al.*, Phys. Rev. B **89**, 224109 (2014).

24. M. D. Knudson and M. P. Desjarlais, Phys. Rev. Lett. **103**, 225501 (2009).

25. M. D. Knudson and M. P. Desjarlais, Phys. Rev. B **88**, 184107 (2013).

26. M. A. Barrios, D. G. Hicks, T. R. Boehly, D. E. Fratanduono, J. H. Eggert, P. M. Celliers, G. W. Collins, and D. D. Meyerhofer, Phys. Plasmas **17**, 056307 (2010).

27. M. D. Knudson and R. W. Lemke, J. Appl. Phys. **114**, 053510 (2013).

28. D. G. Hicks, T. R. Boehly, P. M. Celliers, J. H. Eggert, S. J. Moon, D. D. Meyerhofer, and G. W. Collins, Phys. Rev. B **79**, 014112 (2009).

29. M. D. Knudson, M. P. Desjarlais, and A. Pribram-Jones, Phys. Rev. B **91**, 224105 (2015).

30. T. R. Boehly, D. L. Brown, R. S. Craxton, R. L. Keck, J. P. Knauer, J. H. Kelly, T. J. Kessler, S. A. Kumpan, S. J. Loucks, S. A. Letzring, F. J. Marshall, R. L. McCrory, S. F. B. Morse, W. Seka, J. M. Soures, and C. P. Verdon, Opt. Commun. **133**, 495 (1997).

31. S. Skupsky, R. W. Short, T. Kessler, R. S. Craxton, S. Letzring, and J. M. Soures, J. Appl. Phys. **66**, 3456 (1989).

32. Y. Lin, T. J. Kessler, and G. N. Lawrence, Opt. Lett. **20**, 764 (1995).

33. E. I. Moses *et al*., Phys. Plasmas **16**, 041006 (2009).

34. D. E. Fratanduono, D. H. Munro, P. M. Celliers, and G. W. Collins, J. Appl. Phys. **116**, 033517 (2014).

35. P. C. Souers, *Hydrogen Properties for Fusion Energy* (University of California Press, Berkeley, CA, 1986).

36. P. M. Celliers, D. K. Bradley, G. W. Collins, D. G. Hicks, T. R. Boehly, and W. J. Armstrong, Rev. Sci. Instrum. **75**, 4916 (2004).

37. M. C. Gregor, R. Boni, A. Sorce, J. Kendrick, C. A. McCoy, D. N. Polsin, T. R. Boehly, P. M. Celliers, G. W. Collins, D. E. Fratanduono, J. H. Eggert, and M. Millot, Rev. Sci. Instrum. **87**, 114903 (2016).

38. A. Lazicki, R. A. London, F. Coppari, D. Erskine, J. Hawreliak, D. Fratanduono, P. Celliers, J. Eggert, M. Millot, D. Swift, G. Collins, M. Morales, K. Capersen, S. Kucheyev, H. Whitley, J. Caster, and J. Nilsen, "Shock Equation of State of LiH to 1100 GPa," submitted to Physical Review E.

39. P. M. Celliers, G. W. Collins, D. G. Hicks, and J. H. Eggert, J. Appl. Phys. **98**, 113529 (2005).

40. G. I. Kerley, Sandia National Laboratory, Albuquerque, NM, Report SAND2003-3613 (2003).

41. H. F. Robey, T. R. Boehly, P. M. Celliers, J. H. Eggert, D. Hicks, R. F. Smith, R. Collins, M. W. Bowers, K. G. Krauter, P. S. Datte, D. H. Munro, J. L. Milovich, O. S. Jones, P. A. Michel, C. A. Thomas, R. E. Olson, S. Pollaine, R. P. J. Town, S. Haan, D. Callahan, D. Clark, J. Edwards, J. L. Kline, S. Dixit, M. B. Schneider, E. L. Dewald, K. Widmann, J. D. Moody, T. Döppner, H. B. Radousky, A. Throop, D. Kalantar, P. DiNicola, A. Nikroo, J. J. Kroll, A. V. Hamza, J. B. Horner, S. D. Bhandarkar, E. Dzenitis, E. Alger, E. Giraldez, C. Castro, K. Moreno, C. Haynam, K. N. LaFortune, C. Widmayer, M. Shaw, K. Jancaitis, T. Parham, D. M. Holungal, C. F. Walters, B. Haid, E. R. Mapoles, J. Sater, C. R. Gibson, T. Malsbury, J. Fair, D. Trummer, K. R. Coffee, B. Burr, L. V. Berzins, C. Choate, S. J. Brereton, S. Azevedo, H. Chandrasekaran, D. C. Eder, N. D. Masters, A. C. Fisher, P. A. Sterne, B. K. Young, O. L. Landen, B. M. Van Wonterghem, B. J. MacGowan, J. Atherton, J. D. Lindl, D. D. Meyerhofer, and E. Moses, Phys. Plasmas **19**, 042706 (2012).

42. S. Hamel, L. X. Benedict, P. M. Celliers, M. A. Barrios, T. R. Boehly, G. W. Collins, T. Döppner, J. H. Eggert, D. R. Farley, D. G. Hicks, J. L. Kline, A. Lazicki, S. LePape, A. J. Mackinnon, J. D. Moody, H. F. Robey, E. Schwegler, and P. A. Sterne, Phys. Rev. B **86**, 094113 (2012).